Research Article

Vol. 3, No. 5/25 October 2025/*Optica Quantum* 445

OPTICA QUANTUM

A single-phonon directional coupler

Amirparsa Zivari,[1,†] **Niccolò Fiaschi,**[1,†] **Lorenzo Scarpelli,**[1,†] **Menno Jansen,**[2,3] **Roel Burgwal,**[2,3] **Ewold Verhagen,**[2,3] **and Simon Gröblacher**[1,*]

[1] *Kavli Institute of Nanoscience, Department of Quantum Nanoscience, Delft University of Technology, 2628CJ Delft, The Netherlands*
[2] *Center for Nanophotonics, AMOLF, Science Park 104, 1098XG Amsterdam, The Netherlands*
[3] *Department of Applied Physics and Science Education and Eindhoven Hendrik Casimir Institute, Eindhoven University of Technology, P.O. Box 513, 5600MB Eindhoven, The Netherlands*
[†] *These authors contributed equally to this work.*
**s.groeblacher@tudelft.nl*

Received 3 June 2025; revised 8 September 2025; accepted 9 September 2025; published 6 October 2025

Integrated photonics has revolutionized fields such as telecommunications, quantum optics, and metrology by enabling compact, scalable circuits through highly confined optical modes. Within the field of quantum acoustics, phonons have emerged as a compelling alternative, offering advantages such as lower energy, smaller mode volume, and low propagation speeds, which make them ideal for interfacing diverse quantum systems. Developing integrated phononic circuits is thus essential for unlocking the full potential of quantum acoustics and advancing technologies such as quantum computing and hybrid systems. In this work, we demonstrate the first 4-port directional coupler for quantum mechanical excitations—a key building block for phononic circuits. By tuning the coupling region length, we achieve phononic beam splitters with controllable splitting ratios. We validate quantum-level performance by sending a single-phonon Fock state through the device. This work represents a foundational advance toward scalable, integrated phononic platforms for both classical and quantum applications.

https://doi.org/10.1364/OPTICAQ.569727

1. INTRODUCTION

Quantum technologies have seen rapid progress in the past few years, with great promise for testing fundamental science, as well as for commercial applications. First attempts to achieve quantum computational advantage [1,2] over classical processors and long-distance quantum teleportation using a satellite [3] have highlighted the fundamental need to create heterogeneous quantum systems [4] in order to realize advanced quantum technologies [5], such as quantum networks [6]. Phonons—quantized mechanical vibrations—are regarded as a critical resource to connect different quantum devices [7,8], with applications in, for example, quantum transduction [9–11] and sensing [12]. Accordingly, routing and manipulating single mechanical vibrations on a chip is crucial to transfer quantum information between different quantum systems and unlock the potential of hybrid quantum systems.

However, to date, for quantum information purposes based on traveling phonons, two main platforms have been developed: surface acoustic waves (SAWs) [13–15] and highly confined one-dimensional phononic waveguides based on phononic crystals [16]. In particular, SAWs have been used to couple two qubits to one another over a distance of around 2 mm [13]. The propagation distance of these acoustic waves is however limited by the relatively short phononic lifetime T_1 in the range of tens of microseconds. At the same time, due to the two-dimensional, inherently open nature of SAWs, devices are characterized by a relatively large footprint, making scaling to more complex circuits challenging. Nevertheless, SAW platforms are suitable candidates for coupling single traveling phonons to superconducting qubits, which are deterministic sources and detectors for single phonons, and have been used in various outstanding studies in quantum acoustics. Highly confined traveling GHz phonons in phononic crystal waveguides, on the other hand, are characterized by milliseconds-long lifetimes [16] and feature a relatively small footprint compared to SAWs, making them an ideal platform for on-chip quantum applications [17] and for integrated phononic circuits in general. In these structures, an opto-mechanical resonator is typically used for the generation, manipulation, and detection of highly confined phonons: from realizing single-Fock states of phonons [18,19], remote phonon–phonon quantum entanglement [20], and optomechanical Bell tests [21] to quantum teleportation [22]. More recently, single-phonon waveguides were successfully connected to such opto-mechanical resonators to route single-phonon wavepackets on a chip [17].

In photonics, beam splitters form one of the fundamental building blocks for a myriad of applications—they provide a classical platform to investigate the wave nature of light, are used as combiners and power distributors, are critical for quantum optics experiments, and are an essential resource for linear optical quantum computing and processing [23], to name a few examples. Importantly, the ability to miniaturize photonic components has been paramount for realizing novel technologies, as it enables photonic integrated circuits with thousands of components while still preserving a millimeter-scale footprint [24–26]. Some classical demonstration of beam splitters for GHz phonons have been realized over the past years, showing the growing interest in this topic [27–29]. Additionally, significant progress has recently culminated in a remarkable proof-of-principle demonstration of a phononic beam splitter for SAWs [30] in quantum regime. In close analogy to photonics, here we experimentally realize the phononic equivalent of this crucial component—an integrated phononic beam splitter—one of the most critical elements to perform advanced on-chip manipulation of mechanical excitations, in both classical and quantum regime. Drawing inspiration from photonics, we design our beam splitter using a 4-port directional coupler architecture, where two identical single-mode waveguides are coupled together in an interaction region, creating symmetric and anti-symmetric supermodes which are delocalized in both waveguides. The splitting ratio can be adjusted by changing the length of this interaction region. We demonstrate the beam splitter behavior for both coherent and single-phonon Fock states. With a footprint of only about 200×5 µm, our device is easily scalable and represents a critical step towards the realization of integrated phononic circuits [31–33].

2. DEVICE DESIGN AND CHARACTERIZATION

A conceptual sketch of our device is shown in Fig. 1(a). The device is formed by two single-phonon sources (the optomechanical cavities), two single-mode waveguides, a directional coupler, and two single-phonon detectors. To realize the phononic beam splitter, we design an integrated directional coupler using a phononic crystal architecture. The corresponding unit cell of length a is shown in the inset of Fig. 1(b). It consists of two single-mode waveguides [16], connected together via a phononic bridge. The phononic bridges have a full bandgap at the frequencies of interest. Therefore, the coupling is evanescent and is just a weak perturbation to the uncoupled modes. This interaction region allows mechanical energy to be exchanged between the waveguides, resembling the evanescent coupling typically used in photonic directional couplers. In contrast to a conventional directional coupler, the two waveguides host both the two incoming, as well as the two outgoing ports, as detailed later. To verify the analogy to a photonic directional coupler, we perform finite element simulations of the unit cell using COMSOL and calculate the corresponding band structure. The results are shown in Fig. 1(b), for the breathing mode in the in-plane direction. Within a frequency range of 4.5 – 5.3 GHz, the band structure is dominated by the symmetric and anti-symmetric supermodes, which are the even and odd linear combinations of the uncoupled modes, respectively. This range also defines the operational bandwidth of the current design. A zoom-in around 4.9 GHz shown in Fig. 1(c) reveals that the two supermodes have different propagation constants $\beta_{\mathrm{s,a}}$, which relate, according to conventional coupled mode theory [34], to the coupling coefficient β per unit length as $\beta = (\beta_{\mathrm{s}} - \beta_{\mathrm{a}})/2$, with the subscripts $i = \{\mathrm{s, a}\}$ indicating the symmetric and anti-symmetric supermodes, respectively. As a result of the coupling, for each wave vector, the supermodes are frequency split by the normal mode splitting $\Delta\nu_{\mathrm{NMS}}$, as expected from two coupled degenerate harmonic oscillators. We use the extracted value of β to estimate the coupling length needed for different splitting ratios.

To reduce the experimental complexity, we engineer a device with a (phononic) mirror at the center of Fig. 1(a) (represented by the dashed line, and realized by a free-standing end) [16,17]. In this way the same two cavities can be used as transmitters and receivers. We note that, for temporally distinguishable wavepackets as is the case in our experiments, this is equivalent to having a physical 4-port system. The output arms of the directional coupler are connected to two uncoupled, single-mode waveguides, each terminated with a (nominally identical) optomechanical cavity. The cavities are used to generate and detect single phonons via the optomechanical interaction. Through finite element simulation of the full structure, we can calculate the optomechanical coupling rates for different modes, plotted in Fig. 1(d). The optomechanical response is dominated by a series of Fabry–Pérot modes, equally spaced by $\Delta\nu_{\mathrm{FRS}}$, which arise from the hybridization of the mechanical cavity mode with the series of modes supported by the free-ending waveguide. Furthermore, each Fabry–Pérot mode is split by $\Delta\nu_{\mathrm{NMS}}$ into a doublet due to the mechanical coupling between the two devices (see Supplement 1 for more details). Scanning electron microscope (SEM) pictures of one of the fabricated devices, made from a 250-nm-thick device layer of an SOI wafer [16,17], are shown in Fig. 1(e). For space reasons, the waveguides are not fully shown, and the total length of the device is about 200 µm.

To minimize the thermal noise background, we cool our device to 20 mK using a dilution refrigerator, initializing all mechanical modes of interest in their quantum ground states. We measure the optical characteristics of the two optomechanical cavities by scanning a continuous-wave laser through their resonances and measure the reflected signal on a photodiode. The reflection spectra are shown in Figs. 2(a) and 2(b) (for cavity A and B, respectively). Fitting the line shape with a Lorentzian, we determine the optical cavity resonance at $\lambda \approx 1546.81$ nm ($\lambda \approx 1547.98$ nm), and a full-width at half-maximum (FWHM) of $\kappa/2\pi \approx 1.23$ GHz ($\kappa/2\pi \approx 1.34$ GHz), with an intrinsic loss rate of $\kappa_i/2\pi \approx 430$ MHz ($\kappa_i/2\pi \approx 600$ MHz), for device A (B), respectively. The cavities are nominally identical, apart from fabrication imperfections. Since the difference between the optical resonances is much bigger than the linewidths and mechanical frequencies, we can address each cavity individually. This allows us to measure the mechanical spectrum of the structure using optomechanically induced transparency (OMIT) [35]. The results are plotted in Figs. 2(c) and 2(d) (for cavity A and B, respectively). Both devices, within a region of ~ 30 MHz (highlighted in green shaded area) show a series of doublets with a normal mode splitting of $\Delta\nu_{\mathrm{NMS}} \approx 2.5$ MHz, spaced almost evenly by $\Delta\nu_{\mathrm{FRS}} \approx 10$ MHz. As will be shown later, this is a signature of mode hybridization through the directional coupler and corresponds to a directional coupler with a splitting ratio of approximately 50:50. We further determine the equivalent single photon optomechanical coupling rate from the Stokes scattered photon rate by sending 30 ns optical pulses to the devices. We estimate $g_{0,A} = 380$ kHz and $g_{0,B} = 530$ kHz for device A and B, respectively. We note that these are effective coupling rates, resulting from the coupling rate of all modes excited within the pulse length. Furthermore, the simulated coupling rates shown

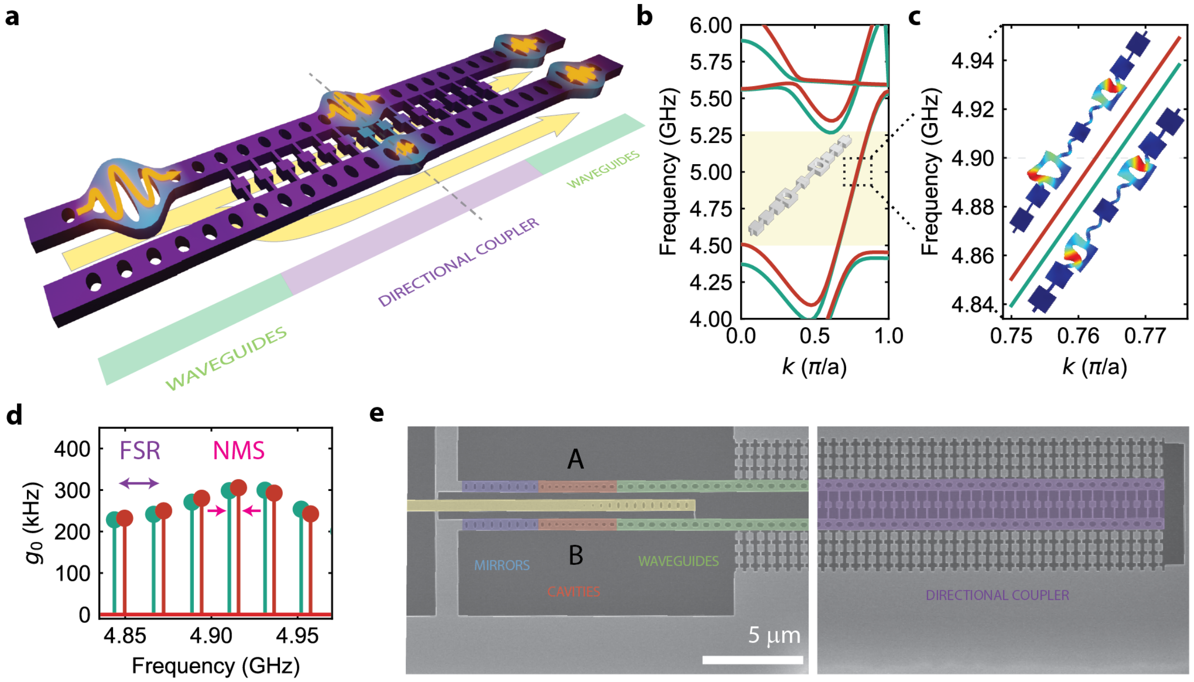

Fig. 1. (a) Sketch of the phononic directional coupler device, which includes two uncoupled phononic waveguides (green) coupled together in the central region (purple). The orange pulses represent classical wavepackets. A wavepacket generated in one of the waveguide splits into two identical wavepackets after transmission through the coupler with a 50:50 spitting ratio. (b) Band structure simulation of the in-plane breathing mode of the unit cell structure (inset) of the directional coupler, showing normal mode splitting of the symmetric (green line) and anti-symmetric (red line) supermodes due to the coupling. (c) The splitting between the two modes is clearly visible in the zoom-in around 4.9 GHz. The oscillating anti-symmetric and symmetric supermodes are shown on the top and bottom, respectively. (d) Simulated optomechanical single photon coupling rate of the full structure. The mechanical mode of the optomechanical cavity is hybridized by a series of Fabry–Pérot modes of the waveguide and each mode is split into a doublet of symmetric (green) and anti-symmetric normal modes (more details are given in Section 1 of Supplement 1). (e) Scanning electron microscope (SEM) images of the fabricated device with false color highlighting of the different parts—the phononic and photonic mirrors (blue), the optomechanical cavities (red), the phononic waveguide (green), and the phononic directional coupler (purple). For a 50:50 splitting, the coupler length is about 26 μm, and the total device length is about 210 μm. Due to space constraints, only a short section of the waveguides is shown.

in Fig. 1(d) are calculated for a shorter device length compared to the measured device (for faster computational run-times) and can therefore not be directly compared to the experimental values.

3. COHERENT DRIVE MEASUREMENT

In order to characterize the time-domain behavior of the beam splitter, we study the propagation of coherent phononic wavepackets. We detune the laser by 6 GHz from the optical cavity we aim to excite. By using this detuning, the Stokes (and anti-Stokes) scattering rate are strongly suppressed and can be neglected. We then modulate sidebands at the mechanical frequency $f_m = 5.31$ GHz onto the laser using an electro-optical modulator (EOM). The sidebands create a beating tone at the mechanical frequency, which coherently drives the mechanical motion through radiation pressure. The optical pulses are created using an acousto-optical modulator and are 30 ns long, such that we excite modes only within the spectral region shown in the green shaded area in Figs. 2(c) and 2(d), for cavity A and B, respectively.

To measure the phonon occupancy inside the cavities A and B, we again use a continuous-wave laser, red-detuned by the mechanical frequency from the optical resonances. The results of the normalized phononic population, with respect to the excited population, in the cavities over time are shown in Fig. 3(b), for different combinations of exciting (first letter on the top right corner of each panel) and reading (second letter on the top right corner of each panel) cavities, as it is depicted in Fig. 3(a)—see Section 6 of Supplement 1 for more details. This device has a coupler length of 50 unit cells, which corresponds to an approx. 50:50 beam splitter. As a result of the directional coupler, the excitation is then split between the two waveguides and reaches the cavities A and B after the first round-trip, with a $\pi/2$ phase difference between the arms. Subsequently, at the second recombination on the coupler region (second round-trip), the excitation travels to the opposite port with respect to the one excited initially. This is due to the fact that the phase difference between our phononic packets in the two arms remains constant while they travel through the waveguides [17]. Due to the slight mismatch of the two waveguide-cavity systems and dispersions in the coupler region caused by the fabrication disorders, the amount of energy populating the opposite cavities is slightly different. We note that despite a longer lifetime in these confined structures, the phononic population dims out after about 700 ns. This is mainly caused by dispersion and mismatch between the two waveguides rather than phononic dissipation. Nevertheless, this does not impose a fundamental limit for loss

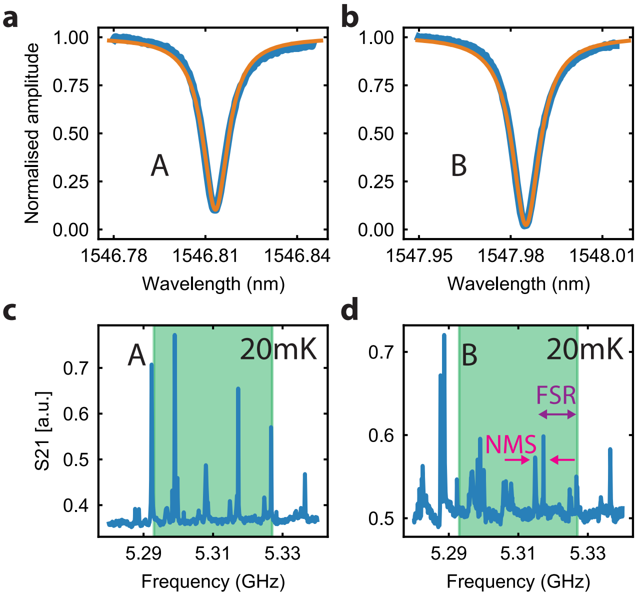

Fig. 2. (a) and (b) Optical response of device A (left) and B (right). The devices have optical resonances in the C-band at telecom wavelengths. (c) and (d) Mechanical spectrum of device A (left) and B (right) measured using OMIT. We observe a series of Fabry–Pérot modes spaced by $\Delta\nu_{\mathrm{FRS}}$ and split by the normal-mode splitting $\Delta\nu_{\mathrm{NMS}}$ due to the directional coupler. The green shaded area indicates the spectral region used to investigate the dynamics of phononic wavepackets (see text for more details).

and can be improved by designing a phononic crystal more robust to disorders and by improving the overall fabrication precision [16,17].

To extract the splitting ratio of the directional coupler, we calculate the (normalized) area under the mechanical wavepacket around the first, second, and third round-trip time, corresponding to the light-blue shaded area in Fig. 3(b), for the indicated excitation and detection combinations (see Section 6 of Supplement 1 for more details). The corresponding integrated counts are shown in blue, orange, green, and red color bars in Fig. 3(c). To model these data, we use a transfer matrix approach, where the action of the directional coupler is described by a lossless beam splitter matrix U_{BS}, written in terms of a reflection coefficient r and a transmission coefficient $t = \sqrt{1 - r^2}$. Phonon losses are negligible to first order since the phononic lifetime is much longer than the round-trip time (see Section 3 of Supplement 1). The phonon population after N passes through the directional coupler is then proportional to $A_{ij}\,(U_{\mathrm{BS}})^N$, where the factor A_{ij}, with $i, j = \{\mathrm{A}, \mathrm{B}\}$, takes into account losses and dispersion mismatch. A more accurate description of these terms would require modeling of the time dynamics with a multi-mode coupled-mode theory, which goes beyond the scope of this work. We then perform a global fitting procedure, where we impose $A_{\mathrm{AB}} = A_{\mathrm{BA}}$ to satisfy the reciprocity condition. The result of the fit is shown in grey color bars in Fig. 3(c), from which we extract a reflection coefficient $R = |r|^2 = 0.43$. We repeat the same measurements for two different lengths of the coupler region (see Section 5 of Supplement 1) and extract the corresponding reflection coefficient. The results are shown in Fig. 3(d), which clearly shows an increase of the reflection as the coupling length is increased. Importantly, these results show that our design allows to engineer phononic beam splitters with arbitrary splitting ratios. We note that we measure negligible reflections at the interface between the uncoupled waveguides and the coupler region (see Section 6 of Supplement 1 for more details).

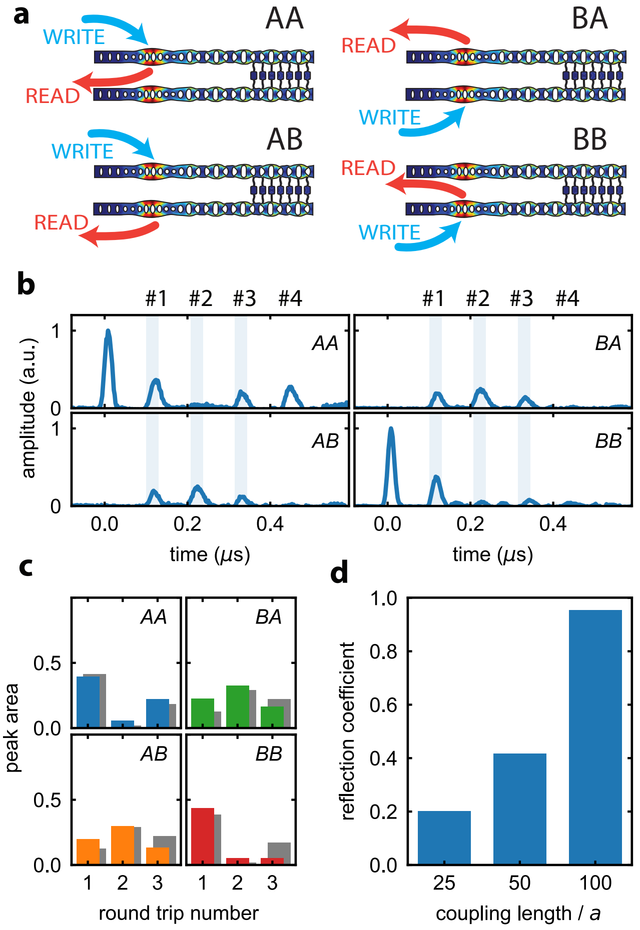

Fig. 3. (a) Different permutations of exciting and reading the two cavities. (b) Normalized phononic population in different cavities with respect to the excited population at t = 0 (first letter: excited cavity, second letter: read-out cavity), using a coherent state phononic wavepacket. The number on the top corresponds to the round-trip number of the phononic packet with the respective time range highlighted in blue. (c) Blue, orange, green, and red color bars: integrated counts of phononic population around the first, second, and third round-trip time, normalized to the amplitude of the peak at zero delay in the excitation waveguide. Grey color bars: result of the global fit described in the main text, from which we extract a reflection coefficient $R = 0.43$. (d) The reflection coefficient of the phononic directional coupler as a function of the coupling length, measured on different devices.

4. SINGLE-PHONON SPLITTING

Due to the relatively low mode frequencies of phonons compared to optical photons in general, and heating induced by optical absorption in optomechanical systems in particular, thermal noise can play a major role in phononic systems, reducing the purity of quantum states, such as single-phonon Fock states. Therefore, going beyond classical demonstrations [29] and testing the response of our directional coupler to quantized excitations with single-phonon wavepackets is a crucial demonstration of its potential use for quantum applications. This becomes even more critical when considering additional phononic losses, for example, via interaction with two-level systems, as well as traveling losses due to dispersion, as all these effects decrease the phononic population compared to the thermal occupancy, thus effectively augmenting decoherence. In this experiment, we excite single-phonon wavepackets in different cavities and detect the reflected signals in both cavities. For a single-phonon input state incident on a beam splitter with a 50:50 splitting ratio, there is an equal 50% chance of receiving a single phonon on either of the output ports.

In order to create a single phonon, we use 30 ns "write" laser pulses, blue-detuned by the central mechanical frequency (5.31 GHz) from the optical resonances. This process can be described by a two-mode squeezed optomechanical interaction, and detecting the Stokes scattered photon with a superconducting nanowire single-photon detector (SNSPD) allows us to project the mechanical state of the optomechanical cavity onto a single-phonon state [18]. This single phonon travels through the waveguide and either returns to the same cavity upon reflection or goes to the opposite cavity after transmission in the coupling region. We then convert the mechanical state of each cavity to an optical photon by sending 30 ns "read" laser pulses red-detuned by the same mechanical frequency from the optical cavities. This addresses a state swap optomechanical interaction resulting in anti-Stokes scattered photons. The time delay between the write and read pulses is set around the first round-trip of the phononic wavepacket. We calculate the second-order cross-correlation $g^{(2)}_{om}$ between the Stokes and anti-Stokes scattered photons for different combinations of exciting and reading cavities A and B, similarly to [18].

We use pulse energies of 220 fJ for write (Stokes) and 280 fJ for read (anti-Stokes) process, corresponding to a Stokes scattering probability of 1 % (1.6 %) and an anti-Stokes scattering probability of 1.2 % (2 %) for cavity A (B). At these low pulse energies, the thermal occupation of the cavities caused by heating of the lasers is negligible ($n_{th} < 0.18$ for all measurement configurations, see Section 4 of Supplement 1). We measure values of $g^{(2)}_{om,AA} = 3.8^{+0.8}_{-0.5}$, $g^{(2)}_{om,AB} = 3.1^{+0.8}_{-0.5}$, $g^{(2)}_{om,BA} = 3.2^{+0.7}_{-0.5}$, and $g^{(2)}_{om,BB} = 3.5^{+0.5}_{-0.5}$ (first index indicating the write cavity and second index the read cavity), which is plotted in Fig. 4. For each configuration, the value is more than two standard deviations above the classical threshold of 2, unambiguously showing the non-classical behavior of the single-phonon states measured in the different cavities after the excitations passed through the coupler region and either return back to the same cavity or travel to the opposite one. We note that these values are consistent with the expected ones for the first round-trip given the thermal occupation and the splitting ratio: $g^{(2)}_{om,exp} \approx (1 + \alpha/n_{th}) \approx 3.7$, with $\alpha = R$ (T) for AA, BB (AB, BA) [16,18]. For more details on the experimental setup, we refer to Sections 5 and 7 of Supplement 1. The equal $g^{(2)}_{om}$ values for different combinations of excitation and detection cavities prove the equal chance of retrieving the phonon in different output ports (i.e. $R = T$), and therefore the 50:50 splitting of a single-phonon state.

A natural next step would be to perform a Hong–Ou–Mandel interference experiment. However, due to the low click rates, the corresponding integration time would currently be prohibitively large. Using different types of optomechanical cavities or a deterministic source of phonons could allow for this experiment [30,36].

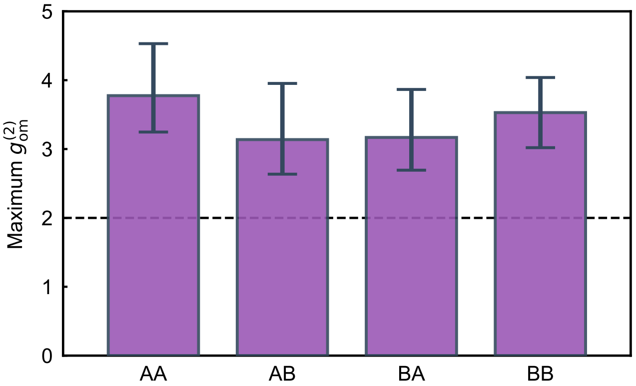

Fig. 4. The second order cross-correlation $g^{(2)}_{om}$ between the Stokes and anti-Stokes scattered photons from the write and read pulses—we measure $g^{(2)}_{om,AA} = 3.8^{+0.8}_{-0.5}$, $g^{(2)}_{om,AB} = 3.1^{+0.8}_{-0.5}$, $g^{(2)}_{om,BA} = 3.2^{+0.7}_{-0.5}$, and $g^{(2)}_{om,BB} = 3.5^{+0.5}_{-0.5}$—all values are above the classical threshold of 2 (dashed line) by more than two standard deviations. Error bars indicate one standard deviation.

5. CONCLUSION

In conclusion, we have demonstrated an integrated directional coupler for GHz phonons—a crucial component for phononic integrated circuits [37]. Our demonstration is based on the development of the first integrated circuit involving single-phonon sources, detectors, and single-mode waveguides, and we use it to demonstrate a beam splitter for both classical and quantum mechanical states. Importantly, the circuit is fabricated with only one lithographic step. Due to the millisecond-long lifetime of phonons in these structures, as well as the ease of scalability, our device can be readily extended to build multi-mode interferometers of large dimensions, suitable for mechanical boson sampling and, more generally, for linear mechanical quantum computing [2,30]. We would like to note that due to having a passive cooldown/reset protocol for our mechanical oscillators, longer lifetimes would lead to a decrease in the repetition rate of the pulse sequence. Therefore, in order to have reasonable data acquisition times in the milliseconds lifetime regime, the scattering probabilities and click rates must also be increased. This is only possible by having optomechanical devices with lower optical absorption to be able to increase the optical pump powers [19,38–41].

Through further development, piezo-electric materials can be included in our mechanical structure [11,42], enabling electromechanical integrated devices such as, for example, phononic phase shifters [43]. With this powerful new tool at hand, a new paradigm of phononic devices can be realized, including mechanical Mach–Zender interferometers for sensing, switches for routing, and power multiplexers, to name a few, in addition to other more versatile mechanical counterparts of existing photonic technologies [44].

Additionally, using piezo-electric resonators, strong interactions between highly confined GHz phonons and superconducting qubits can be engineered [9]. Moreover, the small mode volume of highly confined phonons achieved with our design allows engineering interactions with nanometer-scale quantum system, such as quantum dots [45] and color centers. Therefore, our directional coupler opens up exciting perspectives for hybrid quantum networks, enabling direct entanglement generation between distinct quantum systems without requiring entanglement swapping. We envision a platform with several quantum resources linked and combined together through mechanical quantum channels, taking advantage of the best performances of each individual technology. Our design, based on one-dimensional waveguides, resembles the one of a photonic integrated circuit. Together with the demonstration of non-classical behavior, our work paves the way towards expanding the new field of integrated quantum phononics.

Funding. European Research Council (101001005); Netherlands Organization for Scientific Research (680-92-18-04, NWO Frontiers of Nanoscience program).

Acknowledgment. We would like to thank the Kavli Nanolab Delft for nanofabrication assistance. This work is financially supported by the European Research Council (ERC CoG Q-ECHOS, 101001005) and is part of the research program of the Netherlands Organization for Scientific Research (NWO), supported by the NWO Frontiers of Nanoscience program, as well as through a Vrij Programma (680-92-18-04) grant. A.Z., L.S., N.F., and S.G. devised and planned the experiment. A.Z., N.F, M.J., and R.B. simulated and designed the device. A.Z. and L.S. fabricated the sample, A.Z., L.S., and N.F. built the setup and performed the measurements. A.Z., L.S., and S.G. analyzed the data and wrote the manuscript with input from all authors. E.V. and S.G. supervised the project.

Disclosures. The authors declare no competing interests.

Data availability. Source data for the plots are available on Zenodo [46].

Supplemental document. See Supplement 1 for supporting content.

REFERENCES

1. F. Arute, K. Arya, R. Babbush, *et al.*, "Quantum supremacy using a programmable superconducting processor," Nature **574**, 505–510 (2019).
2. H.-S. Zhong, H. Wang, Y.-H. Deng, *et al.*, "Quantum computational advantage using photons," Science **370**, 1460–1463 (2020).
3. J.-G. Ren, P. Xu, H.-L. Yong, *et al.*, "Ground-to-satellite quantum teleportation," Nature **549**, 70–73 (2017).
4. M. Wallquist, K. Hammerer, P. Rabl, *et al.*, "Hybrid quantum devices and quantum engineering," Phys. Scr. **T137**, 014001 (2009).
5. G. Kurizki, P. Bertet, Y. Kubo, *et al.*, "Quantum technologies with hybrid systems," Proc. Natl. Acad. Sci. USA **112**, 3866–3873 (2015).
6. H. J. Kimble, "The quantum internet," Nature **453**, 1023–1030 (2008).
7. P. Delsing, A. N. Cleland, M. J. A. Schuetz, *et al.*, "The 2019 surface acoustic waves roadmap," J. Phys. D Appl. Phys. **52**, 353001 (2019).
8. S. Barzanjeh, A. Xuereb, S. Gröblacher, *et al.*, "Optomechanics for quantum technologies," Nat. Phys. **18**, 15–24 (2022).
9. M. Mirhosseini, A. Sipahigil, M. Kalaee, *et al.*, "Superconducting qubit to optical photon transduction," Nature **588**, 599–603 (2020).
10. W. Jiang, C. J. Sarabalis, Y. D. Dahmani, *et al.*, "Efficient bidirectional piezo-optomechanical transduction between microwave and optical frequency," Nat. Commun. **11**, 1166 (2020).
11. M. J. Weaver, P. Duivestein, A. C. Bernasconi, *et al.*, "An integrated microwave-to-optics interface for scalable quantum computing," Nat. Nanotechnol. (2023).
12. F. Fogliano, B. Besga, A. Reigue, *et al.*, "Ultrasensitive nano-optomechanical force sensor operated at dilution temperatures," Nat. Commun. **12**, 4124 (2021).
13. A. Bienfait, K. J. Satzinger, Y. P. Zhong, *et al.*, "Phonon-mediated quantum state transfer and remote qubit entanglement," Science **364**, 368–371 (2019).
14. A. Bienfait, Y. P. Zhong, H. S. Chang, *et al.*, "Quantum erasure using entangled surface acoustic phonons," Phys. Rev. X **10**, 21055 (2020).
15. R. P. G. McNeil, M. Kataoka, C. J. B. Ford, *et al.*, "On-demand single-electron transfer between distant quantum dots," Nature **477**, 439–442 (2011).
16. A. Zivari, R. Stockill, N. Fiaschi, *et al.*, "Non-classical mechanical states guided in a phononic waveguide," Nat. Phys. **18**, 789–793 (2022).
17. A. Zivari, N. Fiaschi, R. Burgwal, *et al.*, "On-chip distribution of quantum information using traveling phonons," Sci. Adv. **8**, eadd2811 (2022).
18. R. Riedinger, S. Hong, R. A. Norte, *et al.*, "Non-classical correlations between single photons and phonons from a mechanical oscillator," Nature **530**, 313–316 (2016).
19. S. Hong, R. Riedinger, I. Marinković, *et al.*, "Hanbury Brown and Twiss interferometry of single phonons from an optomechanical resonator," Science **358**, 203–206 (2017).
20. R. Riedinger, A. Wallucks, I. Marinković, *et al.*, "Remote quantum entanglement between two micromechanical oscillators," Nature **556**, 473–477 (2018).
21. I. Marinković, A. Wallucks, R. Riedinger, *et al.*, "An optomechanical Bell test," Phys. Rev. Lett. **121**, 220404 (2018).
22. N. Fiaschi, B. Hensen, A. Wallucks, *et al.*, "Optomechanical quantum teleportation," Nat. Photon. **15**, 817–821 (2021).
23. E. Knill, R. Laflamme, and G. J. Milburn, "A scheme for efficient quantum computation with linear optics," Nature **409**, 46–52 (2001).
24. J. Wang, F. Sciarrino, A. Laing, *et al.*, "Integrated photonic quantum technologies," Nat. Photon. **14**, 273–284 (2020).
25. X. Liu, A. W. Bruch, and H. X. Tang, "Aluminum nitride photonic integrated circuits: from piezo-optomechanics to nonlinear optics," Adv. Opt. Photon. **15**, 236–317 (2023).
26. Y. Wang, J. A. Holguín-Lerma, M. Vezzoli, *et al.*, "Photonic-circuit-integrated titanium: sapphire laser," Nat. Photon. **17**, 338–345 (2023).
27. F. M. Mayor, W. Jiang, C. J. Sarabalis, *et al.*, "Gigahertz phononic integrated circuits on thin-film lithium niobate on sapphire," Phys. Rev. Appl. **15**, 014039 (2021).
28. Q. Zhang, D. Lee, L. Zheng, *et al.*, "Gigahertz topological valley Hall effect in nanoelectromechanical phononic crystals," Nat. Electron. **5**, 157–163 (2022).
29. Z. Feng, Y. Liu, X. Xi, *et al.*, "Gigahertz phononic integrated circuits based on overlay slot waveguides," Phys. Rev. Appl. **19**, 064076 (2023).
30. H. Qiao, É. Dumur, G. Andersson, *et al.*, "Splitting phonons: building a platform for linear mechanical quantum computing," Science **380**, 1030–1033 (2023).
31. K. Fang, M. H. Matheny, X. Luan, *et al.*, "Optical transduction and routing of microwave phonons in cavity-optomechanical circuits," Nat. Photon. **10**, 489–496 (2016).
32. R. N. Patel, Z. Wang, W. Jiang, *et al.*, "Single-mode phononic wire," Phys. Rev. Lett. **121**, 040501 (2018).
33. G. Madiot, R. C. Ng, G. Arregui, *et al.*, "Optomechanical generation of coherent GHz vibrations in a phononic waveguide," Phys. Rev. Lett. **130**, 106903 (2023).
34. W.-P. Huang, "Coupled-mode theory for optical waveguides: an overview," J. Opt. Soc. Am. A **11**, 963–983 (1994).
35. S. Weis, R. Rivière, S. Deléglise, *et al.*, "Optomechanically induced transparency," Science **330**, 1520–1523 (2010).
36. G. S. MacCabe, H. Ren, J. Luo, *et al.*, "Nano-acoustic resonator with ultralong phonon lifetime," Science **370**, 840–843 (2020).
37. W. Fu, Z. Shen, Y. Xu, *et al.*, "Phononic integrated circuitry and spin–orbit interaction of phonons," Nat. Commun. **10**, 2743 (2019).
38. A. Wallucks, I. Marinković, B. Hensen, *et al.*, "A quantum memory at telecom wavelengths," Nat. Phys. **16**, 772–777 (2020).
39. H. Ren, M. H. Matheny, G. S. MacCabe, *et al.*, "Two-dimensional optomechanical crystal cavity with high quantum cooperativity," arXiv (2019).
40. M. Borselli, T. J. Johnson, and O. Painter, "Measuring the role of surface chemistry in silicon microphotonics," Appl. Phys. Lett **88**, 131114 (2006).
41. L. Chen, A. R. Korsch, C. M. Kersul, *et al.*, "Bandwidth-tunable telecom single photons enabled by low-noise optomechanical transduction," arXiv (2024).
42. W. Jiang, F. M. Mayor, S. Malik, *et al.*, "Optically heralded microwave photon addition," Nat. Phys. **19**, 1423–1428 (2023).

43. J. C. Taylor, E. Chatterjee, W. F. Kindel, *et al.*, “Reconfigurable quantum phononic circuits via piezo-acoustomechanical interactions,” Npj Quantum Inf. **8**, 19 (2022).
44. H. Tian, J. Liu, A. Siddharth, *et al.*, “Magnetic-free silicon nitride integrated optical isolator,” Nat. Photon. **15**, 828–836 (2021).
45. C. Spinnler, G. N. Nguyen, Y. Wang, *et al.*, “A quantum dot coupled to a suspended-beam mechanical resonator: from the unresolved- to the resolved-sideband regime,” arXiv (2023).
46. A. Zivari, N. Fiaschi, L. Scarpelli, *et al.*, “Data from: A single-phonon directional coupler,” Zenodo (2025).